From dynamics to statistical mechanics in the Hénon-Heiles model: Dynamics

B. I. Henry
Department of Applied Mathematics, School of Mathematics, The University of New South Wales, P. O. Box 1, Kensington, New South Wales, Australia

J. Grindlay
Guelph-Waterloo Program for Graduate Work in Physics, Waterloo Campus, Physics Department, University of Waterloo, Waterloo, Ontario, Canada N2L 3G1

(Received 30 August 1993)

The equations of motion of the Hénon-Heiles model have been numerically integrated for 100 different starting conditions on the critical energy surface $E=\frac{1}{6}$. The truncation error in the data was monitored using the separation in phase space of two numerical histories with the same initial conditions, based on different time steps, $h=2^{-13}$ and $h'=2^{-14}$. From the data for which the truncation error is less than 1% it is found that the 100 histories fall into three categories, (a) regular (or quasiperiodic), (b) irregular (or chaotic), and (c) regular-irregular. The three-dimensional phase space portraits prove to be the most useful tool in distinguishing between regular and irregular behavior. In category (c) the orbit switches reversibly from (to) regular to (from) irregular behavior. The data suggest that *all* 100 orbits, followed for long enough times, will show regular-irregular behavior and moreover the phase points in these orbits will spend, on average, equal amounts of time in the quasiperiodic and chaotic regimes.

PACS number(s): 05.45.+b

I. INTRODUCTION

The relationship between the irreversible approach to equilibrium or relaxation in macroscopic systems and the reversible dynamical properties of the microscopic constituents has been a long standing problem in nonequilibrium statistical mechanics [1–3]. Typically the interaction between the microscopic particles is described by a Hamiltonian $\mathcal{H}$, with N degrees of freedom, say. The resulting equations of motion generate trajectories in the $2N$ dimensional phase or Γ space. The problem is then to explain macroscopic relaxation in terms of the behavior of these trajectories. In attempting to identify an approach to equilibrium in an isolated Hamiltonian model with energy E, the strategy has been to look for one of two characteristic relaxation properties in the behavior of the trajectory; these are (a) ergodicity, the exploration of most of the energy surface $\mathcal{H}=E$ by a typical trajectory, and (b) equipartition of energy, the distribution in time of E over all the modes of the system. To date the only models amenable to algebraic analysis are those with integrable or near integrable Hamiltonians. Unfortunately the integrability condition means that the system possesses constants of the motion (in addition to energy) or isolating integrals which rule out ergodicity and equipartition. (The isolating integrals define new noninteracting modes.) Similar remarks may be made in the near integrability case by an appeal to the Kol'mogorov-Arnold-Moser [4]. The failure of the algebraic approach emphasizes the importance of numerical studies in the investigation of relaxation in Hamiltonian systems. However, numerical analyses are not without their problems. First of all the capacity of present day computers restricts the analysis to at best a few thousand particles—a far cry from Avogadro's number in macroscopic systems; however, one might hope that a study of small systems could provide some insight into the thermodynamic limit problem. Second, on a more practical level, the trajectories of particular interest are chaotic and so the question of numerical errors and finite size effects must be carefully addressed before the relationship between the numerical results and the long time dynamical behavior of the model can be established.

We have previously reported a numerical investigation of the approach to equilibrium in a 17 particle chain with linear and cubic nearest neighbor forces [5–8], the so called 15+2 model. There are two kinds of difficulties in looking for evidence of relaxation in this model. First, because of the chaotic nature of the trajectories, truncation and roundoff errors rapidly contaminate the numerical integration data for the dynamical histories; as a result we are restricted to analyzing short histories. Second, the chain contains a small number of particles, so that fluctuations in physical quantities, such as the mode energies, are large. These fluctuations make it difficult to determine if a relaxation to equilibrium has taken place and the short histories make it difficult to identify an equilibrium state. To get around both of these problems we adopted the statistical mechanics concept of an ensemble and calculated the trajectories for 101 different starting conditions but a common total energy. These data constitute a numerical ensemble. The set of initial points occupies a small region of the energy surface in Γ space; in the course of time the trajectories explore a larger area of the energy surface. We can view this calculation as a numerical realization of Gibbs's ink drop experiment [9]. The extent of mixing of the trajectories is monitored by calculating the time dependent coarse

 ©1994 The American Physical Society

grained distribution functions and the corresponding Boltzmann H functions for a number of quantities of physical interest. As the ensemble evolves in time, each H function reaches a minimum and maintains this value, aside from *small* fluctuations. We take this as evidence for a relaxation to equilibrium. In the equilibrium state the coarse grained distributions for subsystems (collections of modes with the same frequency) of the constant energy ensemble proved to have the canonical ensemble forms familiar in equilibrium statistical mechanics (ESM). To our knowledge this was the first report in the literature of ESM distributions describing dynamical trajectories of small systems of particles. This finding confirms Gibbs's original proposition: "The laws of statistical mechanics apply to conservative systems of any number of degrees of freedom and are exact" [10]. In contrast to the case described below the 100 trajectories in this ensemble formed a homogeneous group, in as much as, for any physical property, the coarse grained distribution along a trajectory was common to all trajectories.

The Hénon-Heiles model [11] is a Hamiltonian system of order 2. It is an excellent candidate for the exploration of the relationship between dynamical and statistical mechanics for the following reasons: (a) the model is only near integrable at low energies and at larger (but still bound system) energies it is nonintegrable [12]; (b) the phase space trajectories of many initial starting points explore the energy surface [4,11,13], i.e., appear to be ergodic; and (c) the Hénon-Heiles Hamiltonian describes the simplest nontrivial model of a solid—it represents the center of mass reduction of a three particle periodic chain with linear and quadratic forces [13]. In this and a subsequent paper we describe the results of an investigation of relaxation in the Hénon-Heiles model using the numerical ensemble approach described above. We find, as in the 15+2 case, that the Hénon-Heiles model relaxes to equilibrium. However, unlike the 15+2 chain, the set of 100 histories in our ensemble is not homogeneous. Each trajectory falls into one of three categories, (a) regular or quasiperiodic, (b) irregular or chaotic, and (c) regular-irregular. Coarse grained distribution functions for (a) and (b) trajectories give Boltzmann H functions which show relaxation to equilibrium—the relaxation time and the equilibrium distributions of the regular orbits prove to be quite different from those of the irregular orbits. The distributions in the latter case coincide with corresponding surface ensemble results, again in agreement with Gibbs's proposition quoted in the preceding paragraph.

In this paper we describe the numerical methods used to generate and categorize the 100 elements of our ensemble. In a subsequent paper we shall report evidence for relaxation and the consequent equilibrium distributions in this ensemble.

Section II contains a description of the Hénon-Heiles Hamiltonian and some general properties of the model orbits. The numerical integration and the identification of truncation errors are discussed in Sec. III. The properties of the three categories of orbits (a), (b), and (c), see above, are dealt with in Secs. IV, V, and VI: the three dimensional phase portrait proves to be particularly useful in the categorization process. Section VII contains a discussion and summary of our results.

II. MODEL

The Hénon-Heiles Hamiltonian is [11]

$$\mathcal{H}=\tfrac{1}{2}(v_x^2+v_y^2+x^2+y^2)+x^2y-\tfrac{1}{3}y^3 , \tag{1}$$

where $v_x \equiv \dot{x}$ and $v_y \equiv \dot{y}$; this second order Hamiltonian describes the motion of a particle in a two dimensional potential field $V=(x^2+y^2)/2+x^2y-y^3/3$. The motion of the particle becomes unbounded if the system energy E exceeds $\frac{1}{6}$. The equations of motion for the Hamiltonian in (1) are

$$\dot{v}_x=-x-2xy , \tag{2}$$

$$\dot{v}_y=-y-x^2+y^2 . \tag{3}$$

A solution to these equations of motion is described by four functions of time, viz., $x(t)$, $y(t)$, $v_x(t)$, and $v_y(t)$. These four quantities can be thought of as the components of a vector $\mathbf{r}(t)$ in the four dimensional Γ space spanned by x,y,v_x,v_y. Thus a solution $\mathbf{r}(t)$ generates a trajectory or path, the so called dynamical path, in Γ space. The trajectories are reversible in the sense that if $\mathbf{r}(t)$ is a solution, then so is $\mathbf{r}^-\equiv(x(-t),y(-t),-v_x(-t),-v_y(-t))$. While $\mathbf{r}(t)$ and $\mathbf{r}^-(t)$ describe the same path in configuration space (traversed in opposite directions), they describe different paths in Γ space. Since the two dimensional potential field V is symmetric about $x=0$, the $\mathbf{r}(t)$ have a form of inversion symmetry in the sense that if $\mathbf{r}(t)$ is a solution to (2) and (3), then so is $\mathbf{r}^i(t)=(-x(t),y(t),-v_x(t),v_y(t))$; see the Appendix.

Hénon and Heiles [11] numerically integrated these equations for a range of energies $0<E\leq 1/6$ and plotted their data in the form of two dimensional Poincaré surfaces of section (y versus v_y with $x=0$ and $v_x>0$). They interpreted their results as evidence for (a) regular quasiperiodic motion for all initial conditions in the range $E\leq 1/12$ and (b) a mixture of regular quasiperiodic motion for some initial conditions and irregular nonperiodic motion for others in the range $\frac{1}{12}<E\leq\frac{1}{6}$. The fraction of orbits showing irregular behavior varies from zero at $E=\frac{1}{12}$ to very close to one at the critical energy $E=\frac{1}{6}$. The irregular motion, which shows up as an apparently random splatter of points in the Poincaré surface of section, is chaotic [4], i.e., neighboring trajectories separate in time at an average exponential rate. Furthermore it has been suggested that, at the critical energy $E=\frac{1}{6}$, the motion of the system is very nearly ergodic [4,11,13], at least in the approximate sense that at sufficiently long times most single trajectories would visit almost all regions of the surface of sections with equal frequency. However, there has been no quantitative measure of ergodicity reported for the Hénon-Heiles model.

In carrying out numerical experiments designed to measure the chaotic properties of a single chaotic trajectory over very long times we are faced with the immediate difficulties posed by the exponential growth of numerical errors [7]. A prevailing attitude in the literature has

been to discount such errors by appealing to the Anasov-Bowen beta shadow theorem [14,15]. The essence of this theorem is that, while a numerical trajectory will diverge rapidly (exponentially) from the exact trajectory, there exists a different exact trajectory with a slightly different initial point that stays near the numerical trajectory for long times. However, this theorem has only been proved for uniformly hyperbolic systems [14,15] and some other mappings [16,17] and so we have decided to adopt a more conservative approach. Rather than follow a single trajectory over a long time we have chosen to follow the motion of a set of trajectories over times sufficiently short that the separation between the numerical trajectory and the exact trajectory is always less than 1%. As a consequence, the emphasis in our numerical experiments is not to test for ergodicity in the Boltzmann sense [1] but to test for mixing in the Gibbs sense [9]. A feature of our numerical results is that, since the motion of each of the trajectories is reversible, the mixing behavior we shall report in a subsequent paper is also reversible.

III. DYNAMICAL PROPERTIES

We have numerically integrated the equations of motion (2) and (3) for 100 initial conditions, each with the same total energy but different position and velocity coordinates. The starting conditions were chosen to be $E=\frac{1}{6}$, $x(0)=x_j$, $v_x(0)$, $v_x(0)=\dot{x}_j$, $y(0)=0$, and $v_y(0)=0$, where

$$x_j=[2(j-1)/99]1/\sqrt{3}\ ,\quad \dot{x}_j=([\tfrac{1}{3}-x_j^2])^{1/2} \tag{4}$$

for $j=1,2,\ldots,50$,

$$x_{51}=1/\sqrt{3},\quad \dot{x}_{51}=0 \tag{5}$$

and

$$x_{j+51}=x_{51-j}\ ,\quad \dot{x}_{j+51}=-\dot{x}_{51-j} \tag{6}$$

for $j=1,2,\ldots,49$. This set of 100 starting points lies on the semicircle $x^2+v_x^2=\frac{1}{3}$, $x\geq 0$ in the x,v_x plane. Because of the "inversion symmetry" mentioned above, we get no additional, nontrivial, dynamical path information using starting points on the other half circle, $x<0$.

Several test programs were written to integrate the equations of motion (2) and (3) for the starting point $j=1$, using different algorithms (Feynman's half step method, Beeman's fourth order predictor-corrector algorithm, the standard fourth order Runge-Kutta algorithm, and a fifth order Runge-Kutta algorithm), different step sizes (2^{-n}, $n=10,11,12,13,14$), and different numerical precision (double and quadruple). The fifth order Runge-Kutta algorithm [18] proved to be the most accurate within the ranges considered. Although this algorithm does not conserve (pseudo)energy explicitly, as do the symplectic codes of Feynman and Beeman [19], it was found to conserve energy better than these algorithms over the time intervals concerned (up to 2^9 "seconds"). The Runge-Kutta algorithm also has good convergence properties; in the absence of roundoff errors, the numerical trajectory converges to the true or exact trajectory (through the same starting point) as the step size decreases to zero [18]. The equations of motion (2) and (3) were integrated for each of the 100 initial conditions (4)–(6) with two step sizes $h=2^{-13}$ (local truncation error $\approx 10^{-24}$) and $h=2^{-14}$ (local truncation error $\approx 10^{-26}$) for 2^9 s using the fifth order Runge-Kutta algorithm and quadruple precision arithmetic (local roundoff error $\approx 10^{-34}$). The x, y, v_x, and v_y values from the numerical integration with step size $h=2^{-13}$ were stored at 2^{-4} intervals over a period of 2^9 s and the x, y, v_x, and v_y values from the numerical integration with step size $h'=2^{-14}$ were stored at 1-s intervals over the same period. These data constitute a constant energy statistical ensemble for each of the step sizes $h=2^{-13}$ and $h'=2^{-14}$. The calculation required about 100 h CPU time on a Fujitsu VP100.

Thus, for each of the 100 starting conditions we stored two dynamical histories, (sets of points in Γ space), one $\{\mathbf{r}(h,t)\}\equiv\{x(h,t),y(h,t),v_x(h,t),v_y(h,t)\}$ obtained from the integration using the time step $h=2^{-13}$ and the other $\{\mathbf{r}(h',t)\}$ for the smaller time step $h'=2^{-14}$. These two histories are approximations to the exact dynamical path $\mathbf{r}(t)$ passing through a common starting point; $\mathbf{r}(0)=\mathbf{r}(h,0)=\mathbf{r}(h',0)$. Because of truncation error, the approximate paths will increasingly diverge with time from the exact path and from each other. The distance between corresponding approximate points $\mathbf{r}(h,t),\mathbf{r}(h',t)$ in Γ space is denoted by $L(h,h',t)=|\mathbf{r}(h,t)-\mathbf{r}(h',t)|$. Since the integrations have a common starting point, $L(h,h',0)=0$. The maximum possible separation of two points on the energy surface $\mathcal{H}=E$ is the order of $L_0=2\sqrt{2E}$; this gives us an approximate upper bound L_0 for L. Thus when $L<L_0/100$, the h data differ from the more accurate h' data by less than 1%. We adopt $|L/L_0|$ as the measure of truncation error in the h dynamical histories.

Figure 1 contains a plot of $\ln[L/L_0]$ versus t for the case $j=56$. The early part of this curve shows that the two approximations to this orbit $\mathbf{r}(h,t),\mathbf{r}(h',t)$ are separating exponentially. At $t=244$, the truncation error reaches 1% and beyond $t=265$ the error oscillates about

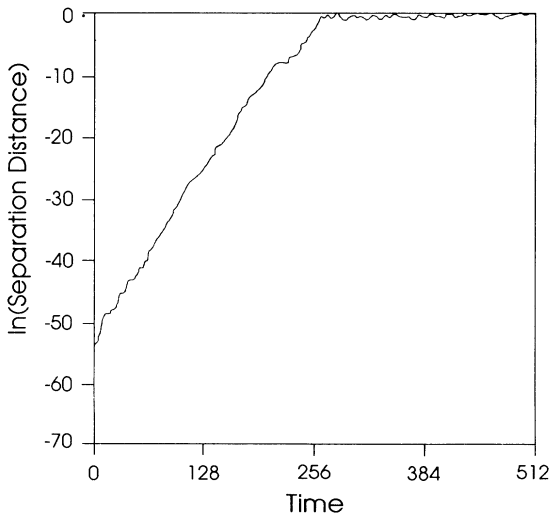

FIG. 1. Graph of $\ln[L(h,h')/L_0]$ versus time for the trajectory labeled $j=56$ and the time steps $h=2^{-13}$ and $h'=h/2$. The dotted line indicates the value ln[0.01].

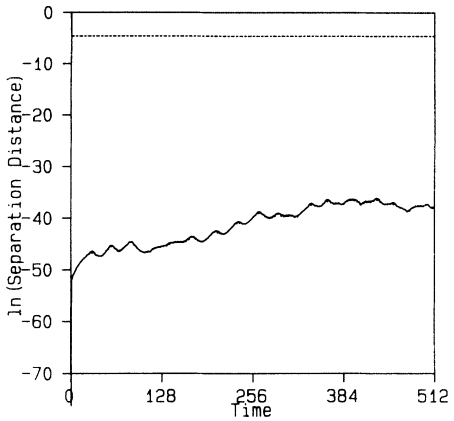

FIG. 2. Graph of $\ln[L(h,h')/L_0]$ versus time for the trajectory labeled $j=28$ and the time steps $h=2^{-13}$ and $h'=h/2$. The dotted line indicates the value ln[0.01].

100%. In contrast the h data conserve the total energy to better than one part in 10^{20} over the full period of 512 s (Fig. 1). The average positive slope of $\ln L$ in the early part of the integration can be identified with the maximum Lyapunov exponent α of the system [20]. From Fig. 1, we find $\alpha=0.21$. Thus, in summary, Fig. 1 shows that (a) our numerical integration data for $j=56$ is accurate to 1% or better only over the first 244 s and (b) the trajectory in this time interval is chaotic or irregular. In contrast, the truncation error graph for the $j=28$ trajectory shows no dramatic increase with time (Fig. 2). In the time interval (0,512) the truncation error remains below 10^{-14}. The truncation error graphs for the remaining 98 histories fall between the extremes of $j=56$ and 28. In half the cases, including $j=56$, the error curve crosses the 1% line before $t=512$. The j values and the corresponding crossover times are listed with increasing crossover times on the three left hand columns in Table I. For the remaining trajectories we have listed the j's in order of increasing value of $|\ln[L/L_0]|$ at $t=512$; see the three right hand columns in Table I. The truncation error graphs for the 100 histories provide us with information on the range of small truncation error; however, they fail to show any clear-cut evidence for the different categories of behavior we report below. Different diagnostic tools are required, namely, three dimensional phase space portraits, two dimensional surfaces of section, and power spectra. We find that the 100 histories can be divided into three categories, (a) regular, (b) irregular, and (c) regular-irregular. We shall describe each category in turn.

IV. REGULAR ORBITS

The four functions $x(t)$, $y(t)$, $v_x(t)$, and $v_y(t)$ describe a dynamical path in Γ space. We have found it useful to plot the path in the three space described by the three functions $x(t)$, $y(t)$, and $v_y(t)$; we shall call these three dimensional phase space portraits. Examples of these portraits are shown in Fig. 3. Here we have broken the $j=28$ data into four equal time segments (0,125), (125,250), (250,375), and (375,500) and plotted the phase

TABLE I. The 100 starting conditions listed in order of increasing 1% crossover time in the left three columns and in order of decreasing $\ln[L(t)/L_0]$ values in the right three columns. The symbols R≡regular, I≡irregular, and i≡possibly irregular are used to describe the nature of the orbit in each of the four 125-s phase portrait windows calculated for the corresponding j value. The numbers in brackets denote multiplicative powers of 10.

Run	Label	1% Crossover	Run	Label	$\ln[L(t=500)/L_0]$
56	IIii	244	32	RRII	−0.538 995 5[1]
54	IIii	256	7	RRRR	−0.838 725 2[1]
50	IIii	266	83	RRII	−0.934 899 1[1]
47	IIii	269	10	RRII	−0.971 861 6[1]
55	IIii	284	81	RRRI	−0.104 300 8[2]
46	IIii	287	96	RRRI	−0.105 748 1[2]
58	IIii	291	25	RRII	−0.133 807 9[2]
34	IIii	294	8	RRII	−0.135 789 5[2]
44	IIIi	306	68	IRRR	−0.152 621 1[2]
62	IIIi	306	89	RRRR	−0.156 129 7[2]
51	IIIi	309	21	RRRI	−0.173 147 4[2]
49	IIIi	322	84	RRRR	−0.186 584 3[2]
45	IIIi	323	91	RRRR	−0.188 176 3[2]
57	IIIi	329	80	RRRR	−0.191 134 6[2]
41	IIIi	331	86	RRRR	−0.194 672 1[2]
40	IIIi	333	19	RRRR	−0.205 426 6[2]
67	IIIi	334	11	RRRI	−0.211 654 4[2]
69	IRIi	344	22	RRRR	−0.217 168 9[2]
48	IIIi	345	5	RRRR	−0.223 113 0[2]
59	IIIi	345	93	RRRR	−0.228 607 1[2]
53	IIIi	347	95	RRRR	−0.230 175 6[2]
33	IIIi	355	92	RRRR	−0.232 272 8[2]
38	IIIi	360	97	RRRR	−0.239 623 8[2]
60	IIIi	364	17	RRRR	−0.243 502 2[2]
30	IIIi	365	6	RRRR	−0.244 171 7[2]
42	RIIi	367	87	RRRR	−0.245 779 7[2]
61	IIIi	368	20	RRRR	−0.258 046 6[2]
64	IIIi	369	3	RRRR	−0.263 625 0[2]
35	IIIi	372	99	RRRR	−0.265 662 5[2]
76	RIIi	380	4	RRRR	−0.266 190 1[2]
31	IIIi	382	13	RRRR	−0.268 019 0[2]
43	IIIi	384	98	RRRR	−0.273 517 5[2]
70	IRIi	390	94	RRRR	−0.273 560 5[2]
52	IIIi	391	29	RRRR	−0.276 156 8[2]
37	IIIi	395	90	RRRR	−0.278 134 9[2]
65	RRIi	399	74	RRRR	−0.279 171 1[2]
72	RIIi	404	18	RRRR	−0.280 959 6[2]
63	IRIi	423	23	RRRR	−0.281 358 6[2]
36	IIII	427	73	RRRR	−0.287 051 2[2]
39	IIRR	428	78	RRRR	−0.288 441 1[2]
27	RRII	430	12	RRRR	−0.291 091 6[2]
77	RIII	440	100	RRRR	−0.295 107 5[2]
82	RIII	448	71	RRRR	−0.300 751 9[2]
24	RIII	450	88	RRRR	−0.305 314 9[2]
79	RIII	459	75	RRRR	−0.306 564 0[2]
2	RRII	465	26	RRRR	−0.312 199 4[2]
66	RIII	476	15	RRRR	−0.326 421 6[2]
1	RRII	481	9	RRRR	−0.335 780 5[2]
85	RRII	482	14	RRRR	−0.349 250 0[2]
16	RRII	491	28	RRRR	−0.373 400 0[2]

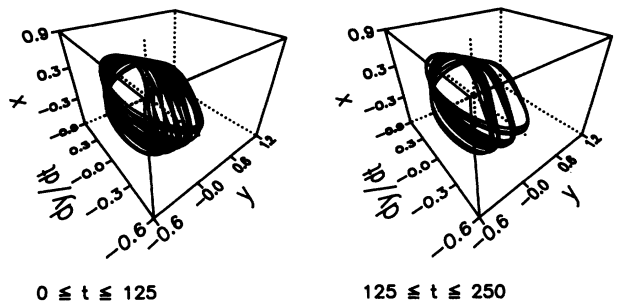

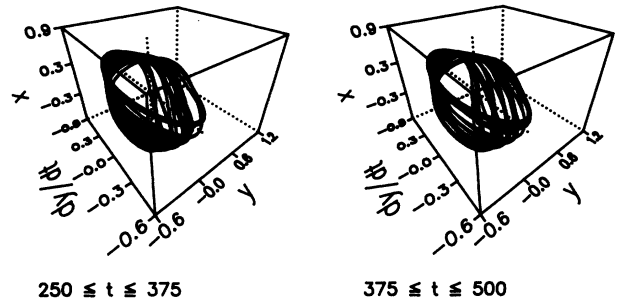

FIG. 3. Three dimensional phase portraits of the trajectory $j=28$ in the four time windows (0,125), (125,250), (250,375), and (375,500). The data were obtained from a numerical integration of (2) and (3) using a time step $h=2^{-13}$.

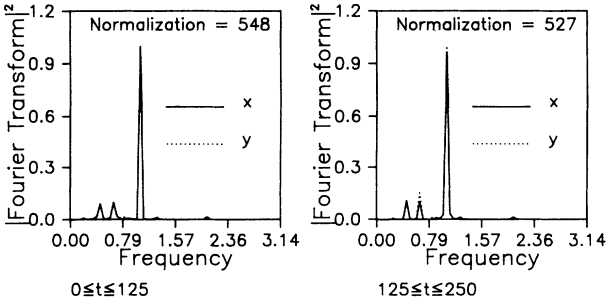

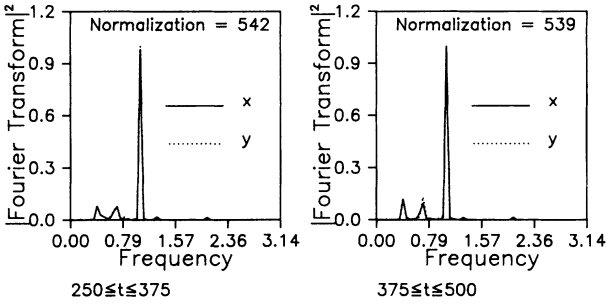

FIG. 5. Power spectra of x and y for the trajectory $j=28$ in the four time windows (0,125), (125,250), (250,375), and (375,500). The data were obtained from a numerical integration of (2) and (3) using a time step $h=2^{-13}$.

portrait in each segment. The $x(t)$, $y(t)$, and $v_y(t)$ path fills similar torus shaped regions in each case. Poincaré surfaces of section (y versus v_y with $x=0$ and $v_x>0$) and power spectra (x and y) [20] for the same $j=28$ trajectory and the same four time segments are shown in Figs. 4 and 5. The major peaks in the power spectra occur at the harmonic frequency $\omega_0=1$. The lack of any evidence for exponentially diverging orbits (Fig. 2), the confinement of the orbit to one region in phase space (Figs. 3 and 4), and the lack of any grassiness in the power spectra (Fig. 5) indicate that this is a quasiperiodic or regular (nonchaotic) orbit. In addition the similarity of behavior in each of the four time segments suggests that at least on this time scale we are not seeing transient behavior. When we examine the analogous truncation error plots, the three dimensional phase space portraits, the Poincaré surface of section, and the power spectra of the remaining 99 trajectories we find that a total of 40 of the 100 trajectories show these regular properties. The regular trajectories are labeled RRRR in Table I. On the semicircle in the v_x,x plane the regular trajectories occur in the two ranges ($3\leq j\leq 29$) and ($71\leq j\leq 100$).

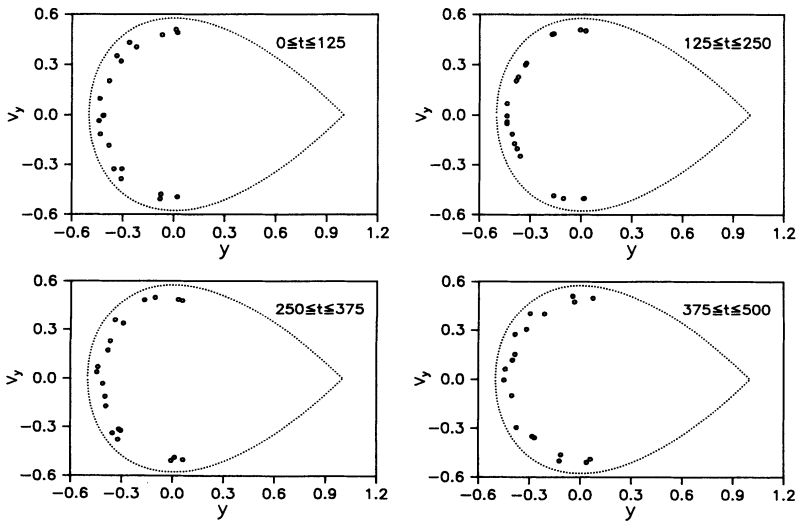

FIG. 4. Poincaré surface of section y versus v_y with $x=0$ and $v_x>0$ for the trajectory $j=28$ in the four time windows (0,125), (125,250), (250,375), and (375,500). The data were obtained from a numerical integration of (2) and (3) using a time step $h=2^{-13}$.

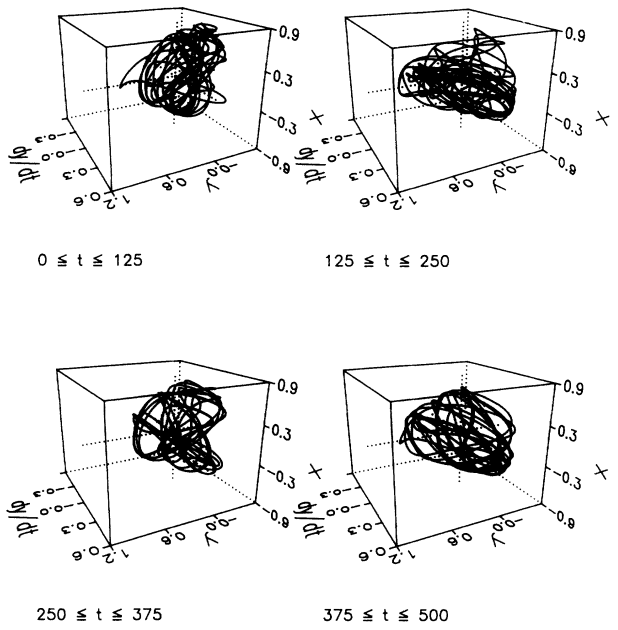

FIG. 6. Three dimensional phase portraits of the trajectory $j=56$ in the four time windows (0,125), (125,250), (250,375), and (375,500). The data were obtained from a numerical integration of (2) and (3) using a time step $h=2^{-13}$.

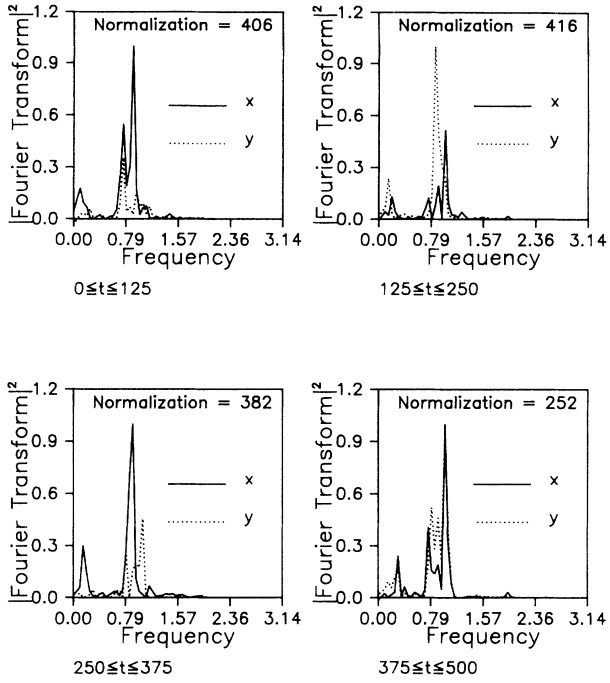

FIG. 8. Power spectra of x and y for the trajectory $j=56$ in the four time windows (0,125), (125,250), (250,375), and (375,500). The data were obtained from a numerical integration of (2) and (3) using a time step $h=2^{-13}$.

V. IRREGULAR ORBITS

Phase space portraits, Poincaré surface of sections, and power spectra for the $j=56$ orbit are shown in Figs. 6, 7, and 8, respectively. Because of the loss of accuracy beyond $t=244$ (see Fig. 1) we shall confine our remarks to the two time segments (0,125) and (125,250). The phase space portraits exhibit spaghettilike intertwining of the $x(t)$, $y(t)$, and $v_y(t)$ paths. Rotations of the axes show no evidence of a torus hole in this tangle. The orbit appears to explore a significant fraction of available phase space in the period (0,250). This is confirmed by the pattern of intersections in the Poincaré surfaces of section. The power spectra (Fig. 8) contain a hint of "grassiness." Thus this orbit shows all the characteristics one associates with chaos, namely, a positive Lyapunov exponent, an unconfined exploration of phase space and grassy power spectra. An examination of the truncation error curves, the phase space portraits, Poincaré surface of sections, and power spectra shows that 32 of the 100 orbits are irregular in this fashion. The orbits are labeled IIII in Table I. We use lowercase to indicate an identification based on a time window in which less than 60% of the points have a truncation error below 1%. The irregular orbits occur only in the range ($30 \leq j \leq 67$).

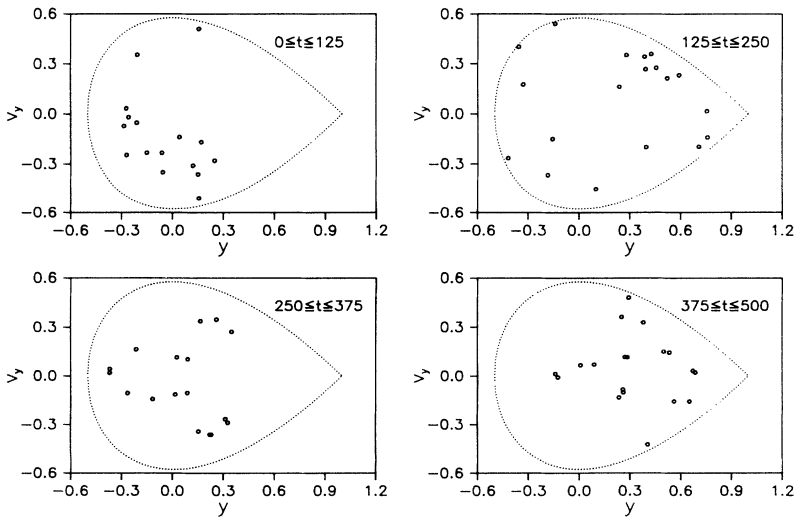

FIG. 7. Poincaré surface of section y versus v_y with $x=0$ and $v_x>0$ for the trajectory $j=56$ in the four time windows (0,125), (125,250), (250,375), and (375,500). The data were obtained from a numerical integration of (2) and (3) using a time step $h=2^{-13}$.

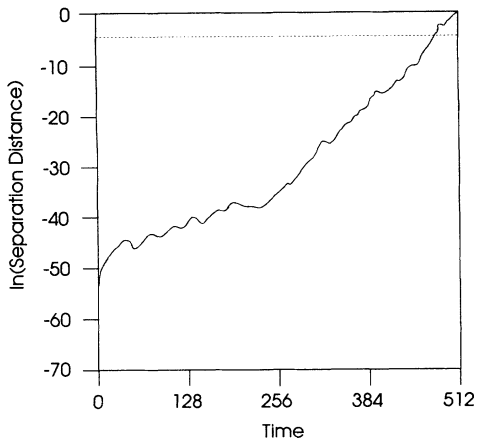

FIG. 9. Graph of $\ln[L(h,h')/L_0)$ versus time for the trajectory labeled $j=1$ and the time steps $h=2^{-13}$ and $h'=h/2$. The dotted line indicates the value ln[0.01].

VI. REGULAR-IRREGULAR ORBITS

The remaining 28 orbits do not fit into either of the two categories above. Consider first the case $j=1$. The truncation error curve is shown in Fig. 9. The change in average slope at about $t=250$ seems to indicate a change in behavior in the orbit. This is much more clearly shown by the set of phase space portraits in Fig. 10. In the first part of the trajectory the two portraits show the torus shape (seen here from the side) of regular motion and, in the later portion, the spaghetti tangle of irregular motion. This change in behavior is confirmed by the corresponding Poincaré surface of sections (Fig. 11) and power spectra (Fig. 12). We label this orbit RRII in Table I. Three points are worth making. First, the truncation error remains below the 1% figure for the full 500 s so that we are not seeing some artifact of computing error. Second, the switch from regular to irregular behavior occurs along an orbit of an isolated system. It is not caused by a change in an external parameter, the usual "route to chaos" reported in the literature (see the case of a Hamiltonian system discussed in Ref. [20]). Third,

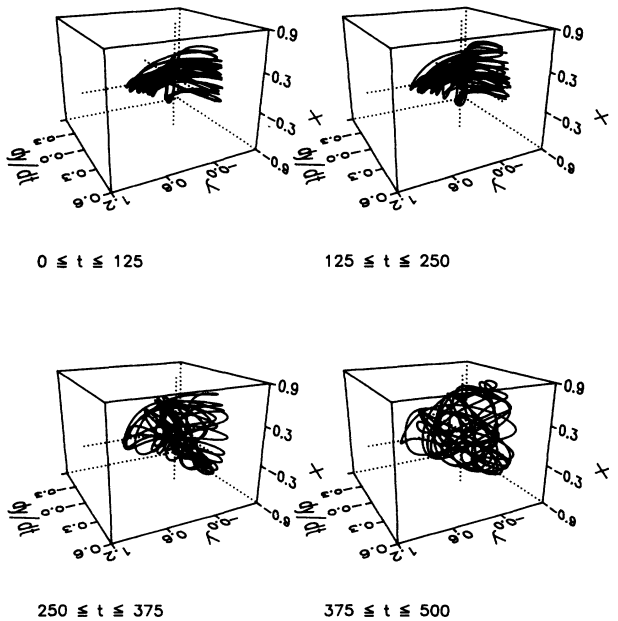

FIG. 10. Three dimensional phase portraits of the trajectory $j=1$ in the four time windows (0,125), (125,250), (250,375), and (375,500). The data were obtained from a numerical integration of (2) and (3) using a time step $h=2^{-13}$.

TABLE II. List of the phase portrait behavior for each j in the range (2,50) and the phase portrait behavior of the corresponding time reversed orbit for j in the range (100,52).

Run	Label	Run
100	RRRRRRII	2
99	RRRRRRRR	3
98	RRRRRRRR	4
97	RRRRRRRR	5
96	IRRRRRRR	6
95	RRRRRRRR	7
94	RRRRRRII	8
93	RRRRRRRR	9
92	RRRRRRII	10
91	RRRRRRRI	11
90	RRRRRRRR	12
89	RRRRRRRR	13
88	RRRRRRRR	14
87	RRRRRRRR	15
86	RRRRRRII	16
85	IIRRRRRR	17
84	RRRRRRRR	18
83	IIRRRRRR	19
82	IIIRRRRR	20
81	IRRRRRRI	21
80	RRRRRRRR	22
79	IIIRRRRR	23
78	RRRRRIII	24
77	IIIRRRII	25
76	iIIRRRRR	26
75	RRRRRRII	27
74	RRRRRRRR	28
73	RRRRRRRR	29
72	iIIRIIIi	30
71	RRRRIIIi	31
70	iIRIRRII	32
69	iIRIIIIi	33
68	RRRIIIii	34
67	iIIIIIIi	35
66	iIIRIIIi	36
65	iIRRIIIi	37
64	iIIIIIIi	38
63	iIRIIIRR	39
62	iIIIIIIi	40
61	iIIIIIIi	41
60	iIIIRIIi	42
59	iIIIIIIi	43
58	iIIIIIIi	44
57	iIIIIIIi	45
56	iiIIIIii	46
55	iiIIIIii	47
54	iiIIIIIi	48
53	iIIIIIIi	49
52	iIIIIIIi	50

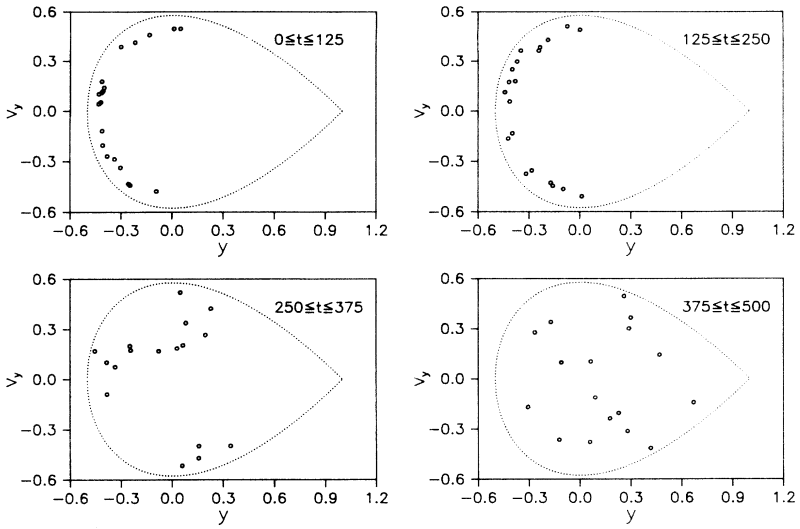

FIG. 11. Poincaré surface of section y versus v_y with $x=0$ and $v_x>0$ for the trajectory $j=1$ in the four time windows (0,125), (125,250), (250,375), and (375,500). The data were obtained from a numerical integration of (2) and (3) using a time step $h=2^{-13}$.

since we are dealing with a reversible dynamical system, there exists a time reversed orbit which we would label IIRR in this 500-s time interval.

The other 26 orbits in this category each exhibit a switch from regular to irregular behavior or the reverse; see Table I. The regular-irregular j values occur throughout the whole range (1,100), with no discernable pattern to their incidence.

Our choice of 125-s time windows was dictated by the need to have sufficient data in each window to be able to characterize the behavior. In the case of a switch over of behavior between two windows it was often clear that the switch occurred within one of the windows. An example of this can be seen in Fig. 10. In the window (250,375) one can see a hint of the to and fro pattern of the previous window, suggesting that the switch takes place after 250 s. By looking at phase space portraits of different choices of windows one could pin down the switch over time more closely than we have done.

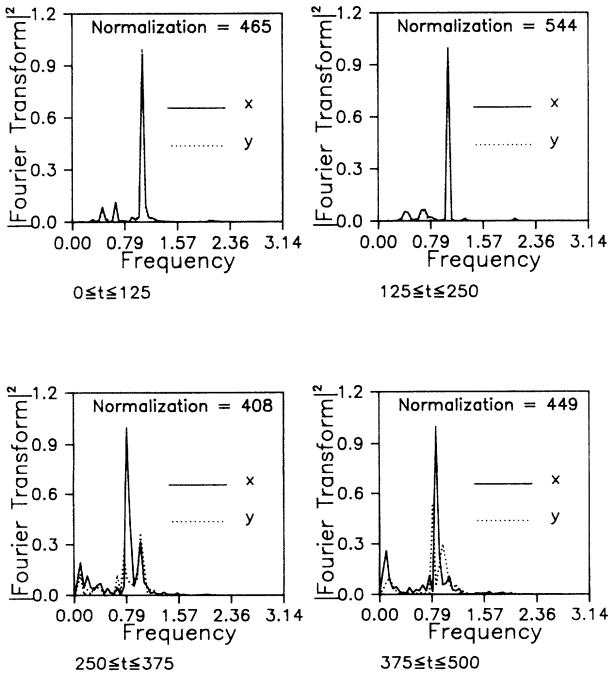

FIG. 12. Power spectra of x and y for the trajectory $j=1$ in the four time windows (0,125), (125,250), (250,375), and (375,500). The data were obtained from a numerical integration of (2) and (3) using a time step $h=2^{-13}$.

VII. DISCUSSION AND SUMMARY

The equations of motion (2) and (3) are time reversible. In the case of our set of 100 orbits, this means that, for example, the time reversed orbit $j=96$ becomes the orbit $j=6$, at $t=0$. Thus the numerical data for $j=96$ (with $v_x\rightarrow -v_x$ and $v_y\rightarrow -v_y$) and $j=6$ can be combined to give a history stretching over 1000 s. In particular, since the pattern for $j=96$ is RRRI and the pattern for $j=6$ is RRRR, the 1000-s pattern is IRRRRRRR. Ninety eight of the histories can be combined in this way. The resulting patterns are shown in Table II. As before the lowercase entries indicate the truncation errors are sufficiently large that the I identification is doubtful. From this table we see the following.

(a) For small j values the trajectories are largely regular with small regions of irregularity; as j increases towards 50 this pattern changes until the irregular behavior dominates.

(b) Of these 49 longer histories, 13 are regular, 12 are irregular, and 24 are regular-irregular. The percentages are 27%, 24%, and 49%, respectively. This compares with the corresponding percentages obtained by treating the 100 orbits as separate entities, namely 40%, 32%, and 28%.

These results suggest that most or all orbits contain regions of regular behavior intermixed with regions of irregular behavior. As further evidence for this speculation we show in Figs. 13 and 14 the truncation error curve and the phase space portraits for the $j=28$ initial conditions (the orbit with the smallest truncation error in Table I), integrated over a period of 1000 s. These graphs show clearly that this orbit switches to chaotic motion at about 750 s. Combining these 1000-s data with the 500-s data of the inversion case, $j=74$, we get the 15 000-s pat-

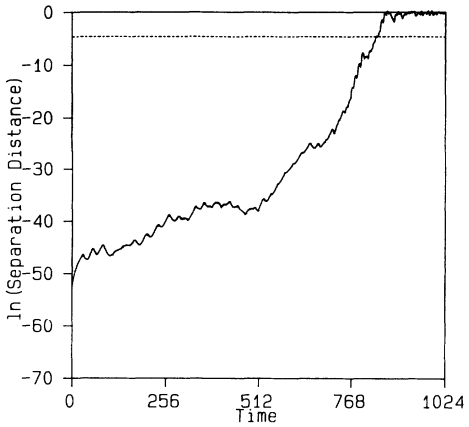

FIG. 13. Graph of $\ln[L(h,h')/L_0]$ versus time for the trajectory labeled $j=28$ over the longer time interval of 1000 s. The time steps $h=2^{-13}$ and $h'=h/2$. The dotted line indicates the value ln[0.01].

tern, RRRRRRRRRRI. A similar test at the other extreme, $j=56$, is clearly not an option because of truncation errors.

We can use the results in Table II to make an estimate of the average over orbits of the percentage of time spent in regular motion. Each entry in the right hand column of Table II represents the behavior in a 125-s time interval. There are 208 regular, 138 irregular, and 46 doubtful irregular for a total of 392 entries. From these numbers we speculate that on average the percentage split between time spent in regular and irregular motion is close to 50%:50%. This is in contradiction to the findings of earlier authors, where the regular behavior is deduced to be a very small fraction of the total [11,13,21]. However, these authors base their conclusions on the Poincaré surface of sections results derived from numerical integrations over periods in excess of 2000 model seconds [22]. The discussion on truncation errors given above suggests that their data represent not an accurate dynamical history of a single orbit on the energy shell $\mathcal{H}=E$ but rather a sequence of shorter accurate histories of different orbits on the same shell [23]. In this interpretation one would then expect that the confined intersections (in the surface of section) of the regular orbits would not show up as such among the scatter of the irregular orbit intersections and so the presence of significant amounts of regular behavior would not be detected.

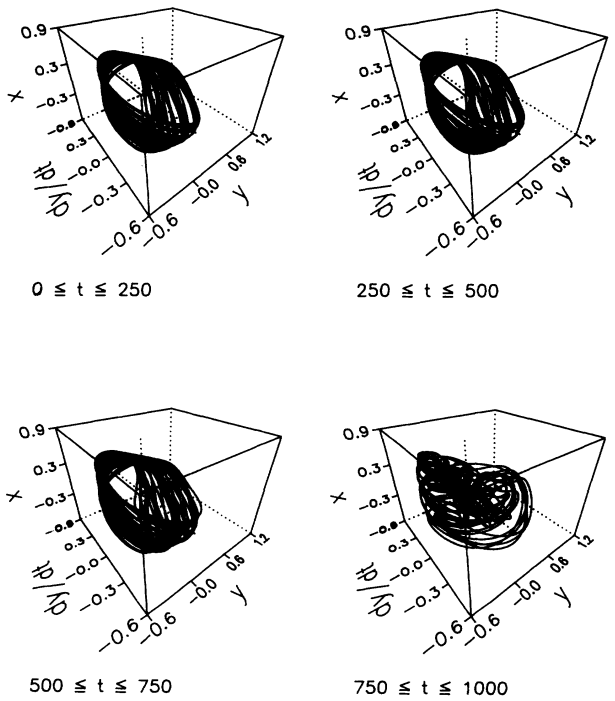

FIG. 14. Three dimensional phase portraits of the trajectory $j=28$ in the four time windows (0.250), (250,500), (500,750), and (750,1000). The data were obtained from a numerical integration of (2) and (3) using a time step $h=2^{-13}$.

In attempting to categorize the 125-s time intervals as R or I, we found in some cases that the Poincaré surface of section results were ambiguous, whereas the three dimensional phase portraits gave a much clearer indication of the classification of the orbit section. This is not surprising when one considers the different natures of the two diagnostic tools. We can use the full number of data points calculated in the time interval (125×16 in our data base) to plot the phase portrait. In contrast only 18–20 points appear in the corresponding surface of section. The advantage of the phase portraits comes from this mass of additional information.

The phase space portraits, Poincaré surface of section and power spectra results for the 40 regular and 32 irregular histories described in Secs. III and IV suggest that in each case we have a group of orbits behaving in a homogeneous fashion, that is to say, in each group the different orbits exhibit similar behavior. These two groups thus provide us with the opportunity to carry out numerical "ink drop" experiments. We shall report the results of this analysis in a subsequent paper.

In summary, we have integrated the equations of motions of the Hénon-Heiles model for 100 different starting conditions on the critical energy surface $E=\frac{1}{6}$. The truncation error in the data was monitored using the separation in phase space of two numerical histories with the same initial conditions and based on different time steps $h=2^{-13}$ and $h'=2^{-14}$. Using the data for which the truncation error is less than 1% we find that the 100 histories fall into three categories, (a) regular (or quasiperiodic), (b) irregular (or chaotic), and (c) regular-irregular. The three dimensional phase space portraits prove to be the most useful tool in distinguishing between regular and irregular behavior. In category (c) the orbit switches reversibly from (to) regular to (from) irregular behavior. We speculate that *all* 100 orbits, followed for long enough times, will show (c) behavior and moreover the phase points in these orbits will spend on average equal amounts of time in the quasiperiodic regimes as the chaotic regime.

ACKNOWLEDGMENTS

This work was supported by the Australian Government and the Natural Sciences and Engineering Council of Canada.

APPENDIX

We now prove the "inversion" property quoted in Sec. II. Consider two points in Γ space $\mathbf{r}=(x,y,v_x,v_y)$ and $\mathbf{r}^i=(-x,y,-v_x,v_y)$ at a time t. $\mathbf{r}^i$ is related to $\mathbf{r}$ via the transformation matrix $\tilde{\mathbf{M}}$, $\mathbf{r}^i=\tilde{\mathbf{M}}\mathbf{r}$, where

$$\tilde{\mathbf{M}}=\begin{bmatrix} -1 & 0 & 0 & 0 \\ 0 & 1 & 0 & 0 \\ 0 & 0 & -1 & 0 \\ 0 & 0 & 0 & 1 \end{bmatrix}.$$

A short time later, $t+\delta t$, $\mathbf{r}$ evolves to

$$\mathbf{r}'=(x+v_x\delta t, y+v_y\delta t, v_x-(x+2xy)\delta t, v_y -(y+x^2-y^2)\delta t)$$

through the equations of motion (2) and (3). Similarly

$$\mathbf{r}^i\rightarrow\mathbf{r}^{i\prime}=(-x-v_x\delta t, y+v_y\delta t, -v_x +(x+2xy)\delta t, v_y-(y+x^2-y^2)\delta t),$$

i.e., $\mathbf{r}^{i\prime}=\mathbf{M}\mathbf{r}'$.

Thus if $\mathbf{r},\mathbf{r}'$ are two points on a dynamical path described by (2) and (3), then $\mathbf{r}^i,\mathbf{r}^{i\prime}$ also lie on a dynamical path.

[1] L. Boltzmann, *Lectures on Gas Theory,* translated by S. G. Brush (University of California Press, Berkeley, 1964) [*Vorlesungen über Gastheorie* (Barth, Leipzig, 1896 and 1898), Pts. I and II, respectively, and references therein].

[2] A. S. Wightman, *Statistical Mechanics at the Turn of the Decade,* edited by E. G. D. Cohen (North-Holland, Amsterdam, 1971), p. 4.

[3] I. Prigogine, *From Being to Becoming—Time and Complexity in the Physical Sciences* (Freeman, New York, 1980).

[4] J. Ford, in *Fundamental Problems in Statistical Mechanics,* edited by E. G. D. Cohen (North-Holland, Amsterdam, 1975), Vol. 3, p. 215.

[5] B. I. Henry and J. Grindlay, Phys. Lett. A **119**, 215 (1986).

[6] B. I. Henry and J. Grindlay, Physica D **28**, 49 (1987).

[7] B. I. Henry and J. Grindlay, Phys. Rev. A **38**, 2594 (1988).

[8] B. I. Henry and J. Grindlay, Phys. Rev. A **40**, 392 (1989).

[9] J. W. Gibbs, *Elementary Principles in Statistical Mechanics* (Yale University Press, New Haven, 1902), p. 147.

[10] J. W. Gibbs, *Elementary Principles in Statistical Mechanics* (Ref. [9]), p. viii.

[11] M. Hénon and C. Heiles, Astron. J. **69**, 73 (1964).

[12] H. Ito, Kodai Math. J. **8**, 120 (1988).

[13] G. H. Lunsford and J. Ford, J. Math. Phys. **13**, 700 (1972).

[14] D. V. Anosov, Proc. Steklov. Inst. Math. **90**, 1 (1967).

[15] R. Bowen, J. Diff. Eqs. **18**, 333 (1975).

[16] S. M. Hammel, J. A. Yorke, and C. Grebogi, J. Complexity **3**, 136 (1987).

[17] S. M. Hammel, J. A. Yorke, and C. Grebogi, Bull. Am. Math. Soc. **19**, 465 (1988).

[18] J. C. Butcher, *The Numerical Analysis of Ordinary Differential Equations: Runge-Kutta and General Linear Methods* (Wiley, Chichester, 1987).

[19] A. R. Janzen and J. W. Leech, Comput. Phys. Commun. **32**, 349 (1984).

[20] S. Ross, J. Grindlay, and B. I. Henry, Phys. Rev. A **44**, 4876 (1991).

[21] V. L. Berdichevsky and M. v. Alberti, Phys. Rev. A **44**, 858 (1991).

[22] We infer this in Refs. [11] and [13], from the average time between Poincaré surface of section intersections in the Hénon-Heiles model, about 7 s, and the number of intersections shown in by these authors.

[23] See the discussion in Sec. III of Ref. [7].